

## Cosmic Ly $\alpha$ Emission from Diffuse Gas

SUNG-HAN TSAI,<sup>1,2</sup> KE-JUNG CHEN,<sup>1</sup> AARON SMITH,<sup>3</sup> AND YI-KUAN CHIANG<sup>1</sup>

<sup>1</sup>*Institute of Astronomy and Astrophysics, Academia Sinica, Taipei 10617, Taiwan*

<sup>2</sup>*Department of Physics, National Taiwan University, Taipei 10617, Taiwan*

<sup>3</sup>*Department of Physics, The University of Texas at Dallas, Richardson, TX 75080, USA*

### ABSTRACT

The Ly $\alpha$  emission has emerged as a powerful tool for probing diffuse gas within the large-scale structure of the universe. In this paper, we investigate cosmic Ly $\alpha$  emission by post-processing cosmological simulations from *IllustrisTNG* and *THESAN* project. Specifically, we calculate the Ly $\alpha$  emission from galaxies, circumgalactic medium (CGM) and intergalactic medium (IGM) across various redshifts. Our results show that IGM alone is significantly under the current observational upper limits. Meanwhile, CGM overshoots the observed galaxy contribution at  $z \lesssim 0.5$  indicating that either the escape fraction for the inner CGM is less than unity or the current photoionization equilibrium treatment with an approximate self-shielding prescription is less accurate. The galaxy component also overshoots at low redshift, indicating that the escape fraction has strong evolution caused by an evolving halo mass function and dust growth distribution, that agrees with observationally inferred escape fractions. Furthermore, our findings suggest that the Ly $\alpha$  emission from diffuse gas (CGM+IGM) peaked at  $z \sim 4$  and diminishes toward lower redshift. The Ly $\alpha$  emission from diffuse gas mainly originates through the collisional excitation of hot plasma. By comparing models with observation, our predicted Ly $\alpha$  emission from diffuse gas remains  $\sim 6$  times fainter than the observed cosmic Ly $\alpha$  emission at  $z = 1 - 3$ . However, future large telescopes may hold great promise to detect Ly $\alpha$  emission from diffuse gas toward  $z > 3$ .

*Keywords:* large-scale structure of universe — Diffuse radiation — Ly $\alpha$  emission — early universe — intergalactic medium

### 1. INTRODUCTION

Modern cosmological simulations based on the  $\Lambda$ CDM model have successfully demonstrated the formation of the large-scale structure (LSS) of the universe (Peebles 1980; Bond et al. 1996; Springel et al. 2005; Wang et al. 2015; McCarthy et al. 2017), including complex processes that produce realistic galaxy populations and their environments (Vogelsberger et al. 2020; Angulo & Hahn 2022). A defining feature of this structure is the cosmic web, characterized by its filaments that act as fundamental building blocks, intricately linking clustered galaxies and extending across the vast cosmic expanse. The hierarchy of filaments channels gas and dark matter to influence the formation and evolution of galaxies within clusters (Dubois et al. 2014; Kraljic et al. 2018; Hasan et al. 2023). The gas that permeates a galaxy cluster, known as the intracluster medium (ICM), holds vital information to understand the thermal and dynamical state of galaxy clusters (Gunn & Gott 1972; Böhringer & Werner 2010; Mantz et al. 2017). The ICM consists mainly of ionized hydrogen and helium and accounts for most of the baryonic material in galaxy clusters. This superheated plasma, with temperature of  $10^7$  to  $10^8$  Kelvin, emits strong X-ray radiation (Tozzi & Norman 2001; Sarazin 1986). Furthermore, the gas around and between galaxies, respectively known as the circumgalactic medium (CGM) and intergalactic medium (IGM), provides insights into the interactions and feedback processes at play (Crain et al. 2009; McQuinn 2016; Tumlinson et al. 2017; Peebles et al. 2019). Despite their crucial role, the extremely low density of CGM and IGM (hereafter referred to as diffuse gas) poses significant observational challenges (Martin et al. 2014; Pakmor et al. 2020). In addition to their extremely low density, the existence of a neutral atomic and molecular CGM component implies that solving the CGM questions requires synergetic optical/UV and sub-mm observations. Unfortunately, none of the current sub-mm telescopes enables such observations (Lee et al. 2024).

Theoretically, the diffuse gas has the potential to emit Lyman-alpha (Ly $\alpha$ ) photons via cascade recombination and collisional excitation mechanisms (Hogan & Weymann 1987; Cantalupo et al. 2005; Rosdahl & Blaizot 2012). However, when the only ionizing radiation source is the cosmic ultra-violet (UV) background, the emitted light is often too faint for direct observation. The detectability of this faint emission significantly increases if the diffuse gas is situated near more energetic sources, such

as quasars, star-forming regions, or supermassive black holes (Charlot & Fall 1993; Steidel et al. 1996; Cantalupo et al. 2005; Umehata et al. 2019a). In these cases, the brightness of Ly $\alpha$  becomes more prominent, enhancing its observability. Alternatively, various technologies are employed to overcome these observational challenges, including stacking subcubes of observational data to achieve higher surface brightness sensitivity levels (Gallego et al. 2018), using integral field unit (IFU) imaging to observe emission from the CGM and IGM (Hu et al. 1991; Hill et al. 2008; Roche et al. 2014; Bacon et al. 2021; Martin et al. 2023), and employing intensity mapping to collect cosmic photons (Chiang et al. 2019; Renard et al. 2024).

In observational studies, there are several factors contribute to the the scarcity of data points, particularly at high redshifts. These factors include background noise, IGM absorption, instrumental limitations, and so on (Tapken et al. 2007; Ouchi 2019). This scarcity poses challenges for investigating and interpreting the evolution of Ly $\alpha$  luminosity density. The limited data, coupled with large error bars, complicates the analysis. To help address this issue, we take a theoretical approach by using the data from large-volume cosmological hydrodynamics simulations provided by the *IllustrisTNG* and *THEASN* projects. By calculating the Ly $\alpha$  emission from these simulations, we compare our predictions with recent observational results and explore the physical properties of Ly $\alpha$  emission at high redshifts. Previous studies have employed these and similar simulations, e.g. focusing on Ly $\alpha$  emitters and halos (Gronke & Bird 2017; Byrohl et al. 2021), LSS clustering properties (Behrens et al. 2018), or prospects of detecting the cosmic web (Elias et al. 2020; Witstok et al. 2021; Byrohl & Nelson 2023), the primary goal of this work is to reconcile the Ly $\alpha$ -visible budget of diffuse gas with local UV background measurements.

In Section 2, we describe the methodology of identifying the diffuse gas in the *IllustrisTNG* and *THEASN* project at  $z < 6$  and calculating their Ly $\alpha$ . In Section 3, we present the physical properties of diffuse gas and its Ly $\alpha$  emission as a function of redshift. Finally, we compare our results with observations and conclude in Section 5.

## 2. METHODS

### 2.1. *The IllustrisTNG project and AREPO code*

The *IllustrisTNG* project comprises large-volume, cosmological, gravo-magnetohydrodynamical simulations that evolve the universe from  $z = 127$  to  $z = 0$  (Pillepich et al. 2018a; Nelson et al. 2018; Naiman et al. 2018; Springel et al. 2018; Marinacci et al. 2018; Nelson et al. 2019a; Pillepich et al. 2019). The primary objective of this project is to deepen our understanding of galaxy formation during cosmic structure evolution. It is achieved by simulating galaxy formation and evolution with high fidelity, facilitating a comprehensive comparison with observed galaxies in our universe.

The *IllustrisTNG* project is executed using the moving mesh code, *AREPO* (Springel 2010). Various physical box sizes, mass resolutions, and microphysics are systematically included in these simulations. This strategic approach enables the exploration of multiple facets of galaxy formation. The workhorse in *IllustrisTNG* simulations is the galaxy formation module (Weinberger et al. 2017; Pillepich et al. 2018b) that contains key physics for modeling galaxy evolution.

#### 2.1.1. *Gas physics and sources of UVB*

The *AREPO* code solves the coupled self-gravity and ideal magnetohydrodynamic (MHD; Pakmor et al. 2011; Pakmor & Springel 2013) equation. Gravitational forces are calculated with the Tree-Particle-Mesh scheme (Xu 1995; Bagla 2002; Bode & Ostriker 2003), which combines the Particle-Mesh method on large scales with a tree code to handle particle-particle interactions at small separations. For MHD, the code employs the finite volume method on a spatial discretization based on an unstructured, moving Voronoi tessellation of the simulation domain. The Voronoi cell tracks the conserved quantities of the fluid in the case of MHD and evolves in time by using Godunov’s method and solving the Riemann problems at cell interfaces (Springel 2010).

To model the galaxy formation and evolution, the simulations in *IllustrisTNG* include the key astrophysical processes, such as star formation, stellar evolution, chemical enrichment, radiative cooling, stellar feedback-driven galactic outflows, and feedback of supermassive black hole (SMBH). However, the grid size of cosmological simulations is much larger than the physical scale of the stellar feedback and the interstellar medium (ISM) turbulence. Therefore, these unresolved baryonic processes are formulated as subgrid models within the *IllustrisTNG* simulations.

#### 2.1.2. *Star Formation and Stellar Feedback*

Galactic star formation is based on Springel & Hernquist (2003), and the criteria for star formation include surpassing a density threshold of  $n_{\text{H}} \approx 0.1 \text{ cm}^{-3}$ . When the gas density exceeds this threshold, stars can form stochastically, following the empirically defined Kennicutt-Schmidt relation with the Chabrier initial mass function (Chabrier 2003). Feedback from unsolved supernovae is considered using a two-phase, effective equation of state model. Stars inject mass, energy, and metal into their surrounding ISM via their asymptotic giant branch (AGB) phase or the supernova explosion, depending on their initial masses. These stellar feedbacks are included in the simulations through tabulated mass and metal yields. The chemistry code follows the

	$L_{box}$ [cMpc/ $h$ ]	$N_{gas,DM}$
TNG50-1	35	2160 <sup>3</sup>
TNG50-2	35	1080 <sup>3</sup>
TNG50-3	35	540 <sup>3</sup>
TNG50-4	35	270 <sup>3</sup>
TNG100-1	75	1820 <sup>3</sup>
TNG100-2	75	910 <sup>3</sup>
TNG100-3	75	455 <sup>3</sup>
TNG300-1	205	2500 <sup>3</sup>
TNG300-2	205	1250 <sup>3</sup>
TNG300-3	205	625 <sup>3</sup>

**Table 1.** Box size and particle number for each TNG simulation run. The Hubble parameter,  $h$  used in TNG simulations 0.68 is based on Planck Collaboration et al. (2016).

evolution of nine elements (H, He, C, N, O, Ne, Mg, Si, and Fe). Cooling functions of metal lines are based on the ISM gas density, temperature, metallicity, and redshift (Smith et al. 2008; Wiersma et al. 2009). The primary radiation source for cosmic gas is the UV background radiation field. However, in regions near the active galactic nuclei (AGNs), this cooling process is also influenced by additional radiation emitted by AGNs (Vogelsberger et al. 2013). The stellar feedback associated with star formation is assumed to drive galactic flows. These outflows are launched directly from star-forming gas, exhibiting an assigned wind velocity corresponding to the local dark matter velocity dispersion (Vogelsberger et al. 2013; Torrey et al. 2014). The wind particles inherit the physical properties of the gas where they are launched, including their thermal energy and metallicity.

### 2.1.3. Feedback of SMBH

The TNG model uses two different schemes to consider the physics of SMBH. In the low-accretion state, it employs a kinetic AGN feedback model, which produces black hole-driven winds. The idea of black hole-driven winds is inspired by recent theoretical arguments regarding the inflow/outflow solutions of advection-dominated accretion flows within this regime (see Yuan & Narayan 2014). For high-accretion rates, the model invokes thermal feedback that heats gas surrounding the black hole.

### 2.1.4. Simulation Selection

The *IllustrisTNG* project consists of simulations conducted across three volumes, each with different mass resolutions. These volumes denoted as TNG50, TNG100, and TNG300, feature cubic lengths of approximately 50, 100, and 300 megaparsecs (Mpc), respectively. Each volume has at least three distinct particle numbers representing various resolutions. The model names of simulations and their input parameters are shown in Table 1. We primarily utilize the TNG100-1 dataset for our study of diffuse gas because it provides a moderate volume that resolves the IGM and CGM with high resolution. Additionally, this dataset includes 14 full snapshots, covering a redshift range from  $z = 6$  to 0, allowing us to examine these structures evolution over time. We use the TNG100-2 dataset to generate the figures that illustrate the distribution of halos, galaxies, CGM, and IGM structures, as well as their Ly $\alpha$  emission in the temperature versus density phase diagram.

## 2.2. The THESAN project

The THESAN project is a suite of large-volume cosmological radiation-magneto-hydrodynamic simulations focused on the epoch of reionization (Smith et al. 2022; Garaldi et al. 2022; Kannan et al. 2022). This project aims to study the processes of cosmic reionization and galaxy formation. It achieves this by combining the *IllustrisTNG* galaxy simulation framework with self-consistent radiation transport, an empirical dust model, and ionizing sources, including binary stellar systems and active galactic nuclei. Like the *IllustrisTNG* project, the simulations are executed using the AREPO code (Springel 2010). The THESAN project provides 80 snapshots with redshifts ranging from 20 to 5.5. In this work, we employ snapshots with redshifts ranging from 6 to 5.5 from the THESAN-1 data as our high redshift constraint. The THESAN project features a box size of 95.5 cMpc on each side. THESAN-1, the highest resolution simulation in the project, employs 2100<sup>3</sup> particles, providing outstanding resolution for investigating the early universe and cosmic reionization processes.

### 2.3. Structure Finding

To define the diffuse gas particles within the `IllustrisTNG` and `THESAN` data, we must exclude gas particles located in the dark matter halos. Nelson et al. (2019b) publicly released the data of the TNG100 and TNG300 on the `IllustrisTNG` project website <sup>1</sup>. To analyze the data, the project provides Friends-of-Friends (FoF) and Subfind algorithms based on Springel et al. (2001) to identify the designated dark matter structures. The FoF algorithm is commonly used to group structured particles in cosmological simulations. It operates by employing a linking length, denoted as  $l$ , where any particle within a distance  $l$  of another particle is linked together to form a group. A particle is linked directly to all other particles within a distance  $l$  and indirectly to all particles that are linked to its friends. This linking process establishes networks of linked particles, known as groups. In the `IllustrisTNG` project, each simulation run employs a linking length of 0.2 in the unit of the mean interparticle separation. Additionally, each group must consist of at least ten particles to be considered. These identified groups are then treated as halos (candidates of galaxy clusters) in cosmological simulations. Subsequently, the Subfind algorithm decomposes each group identified by the FoF algorithm into self-bound subgroups. Each subgroup represents a locally overdense region within the density field of the original structure. They represent individual subhalos (galaxies) within the halo (galaxy cluster) (Springel et al. 2001). The `THESAN` project uses the same approach as `IllustrisTNG` project to identify the structures.

### 2.4. Extracting Diffuse gas

According to the FoF and Subfind algorithms, particles can be categorized into three groups. Firstly, particles excluded by the FoF algorithm are labeled "outer fuzz." These particles exhibit relatively larger separations from each other and disperse throughout the simulation box, away from the FoF regions (halos). They are regarded as intergalactic medium (IGM) particles of the cosmic web within the mock universe. Secondly, particles included by the FoF algorithm but excluded by the Subfind algorithm are labeled as "inner fuzz". Lastly, particles included by both the FoF and Subfind algorithms are referred to as "Subfind" particles. We define the "inner fuzz" particles and the "Subfind" particles with outside 10 per cent of the halo virial radius as the circumgalactic medium (CGM), and treat the remaining as galaxies. The FoF algorithm first identifies halo structures, which are further examined by the Subfind algorithm to identify galaxies within.

Diffuse gas is classified into IGM and CGM components based on whether the particles belong to FoF groups. If a particle is included by the FoF algorithm, it is classified as part of the CGM; otherwise, it is classified as part of the IGM. Figure 1, 2, 3 illustrate the distribution of dark matter, gas, and Ly $\alpha$  emission from the IGM and CGM components within a cube with a side length of 2 cMpc/h at  $z = 1$ . In these plots, we have subtracted the contributions from the host halo with the dark matter mass of  $10^{11} M_{\odot}$ ,  $10^{12} M_{\odot}$ ,  $10^{13} M_{\odot}$  at the center of the box respectively, as well as the contributions from other galaxies in smaller halos. Here, we classify IGM and CGM gas particles as diffuse gas while excluding any particles with a star formation rate (SFR) greater than zero. This approach ensures that we maintain the integrity of the diffuse gas category within our analysis.

In Figures 1 and 2, the CGM distribution reveals that the boxes contain not only a central halo but also other halos, with the IGM connecting these components. In Figure 3, the CGM distribution shows a cluster within the box, with the IGM surrounding the cluster. The CGM components clearly have a higher average density of dark matter and gas and exhibit stronger Ly $\alpha$  compared to the IGM components. These figures demonstrate that the distribution of diffuse gas near different masses' halo can vary significantly.

### 2.5. Calculating Ly $\alpha$ Emissions

We compute the Ly $\alpha$  emission originating from the diffuse gas following the methodology outlined in Smith et al. (2019). We assume that the diffuse gas is optically thin and its Ly $\alpha$  emission originates from collisional excitation and recombination processes. The collisional excitation occurs when a free electron collides with neutral hydrogen and excites the hydrogen's electron to an excited state and subsequently decays from  $2p \rightarrow 1s$ , emitting a Ly $\alpha$  photon. The luminosity of Ly $\alpha$  from collisional exciton,  $L_{\alpha}^{\text{col}}$ , can be expressed as

$$L_{\alpha}^{\text{col}} = h\nu_{\alpha} \int q_{1s2p}(T) n_e n_H dV, \quad (1)$$

where  $h\nu_{\alpha} = 10.2$  eV, the time dependent rate coefficient  $q_{1s2p}(T)$  is taken from Scholz & Walters (1991). The  $n_e$  and  $n_H$  are the number density for the free electron and neutral hydrogen. For the recombination process, a free proton and electron recombine, leaving the electron in any quantum state. Radiative cascades subsequently occur, leading to the production of Ly $\alpha$  photons. The emission can be express as

$$L_{\alpha}^{\text{rec}} = h\nu_{\alpha} \int P_B(T) \alpha_B(T) n_e n_p dV. \quad (2)$$

<sup>1</sup> <https://www.tng-project.org/>

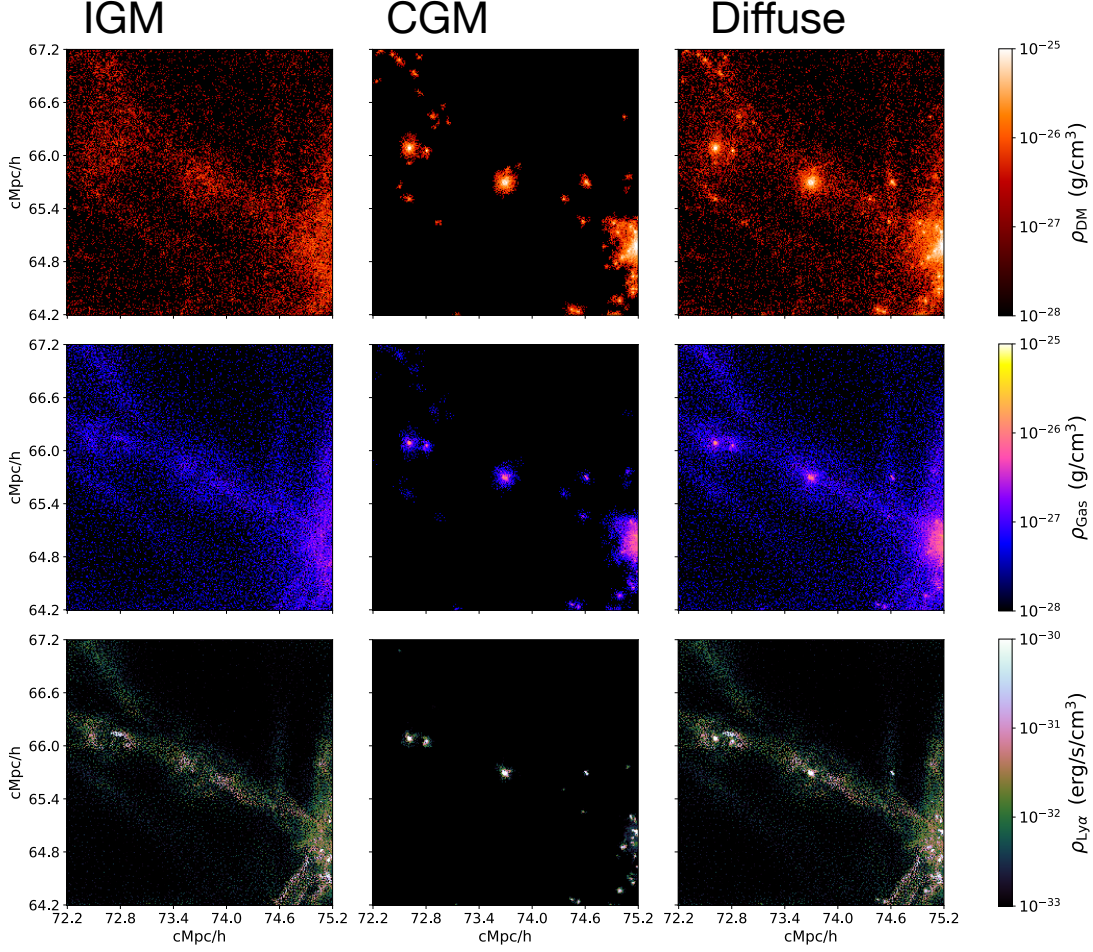


**Figure 1.** The top to bottom rows show the distribution of dark matter, gas, and Ly $\alpha$  emission within a  $1.48 \times 10^{11} M_{\odot}$  dark matter halo, centered in a cube box with a side length of 2 cMpc/h at  $z = 1$ . "IGM" column represents the region of IGM which connect halos throughout the universe, characterized by a lower average density than the CGM. "CGM" column represents the region of CGM, which closely surround galaxies and have stronger emission sources compared to the IGM. "Diffuse" column represents the region of diffuse gas which equals to "IGM" add "CGM" based on our definition.

Here,  $L_{\alpha}^{\text{rec}}$  is the Ly $\alpha$  emission from the recombination process,  $P_B(T)$  represents the Ly $\alpha$  conversion probability per recombination event. For Case-B, where the gas temperature is approximately  $10^4$  K, the  $P_B(T)$  is estimated to be around 0.68 (Cantalupo et al. 2008).  $\alpha_B$  is the recombination coefficient for Case-B, and  $n_p$  is the number density of protons. In Case-B, the  $P_B(T)$  excludes the direction recombination of electron and proton into the ground state and the radiative transitions of the higher order Lyman series such as Ly $\beta$ , Ly $\gamma$ , ... etc.

For particles with a SFR greater than zero, we assume the gas is fully ionized and consider only its recombination processes. These particles typically appear in galaxy regions, though some may be found in the CGM. We treat particles with SFR greater than zero in the CGM region as components of satellite galaxies and consider there Ly $\alpha$  emission as a source of galaxy contribution.

Given the low-density limit of diffuse gas, we also treat Ly $\alpha$  emission from stars as part of the galaxy contribution. To calculate the Ly $\alpha$  emission from stars, we follow the approach outlined in Smith et al. (2022), expressed as

$$L_{\alpha}^{\text{stars}} = 0.68 h \nu_{\alpha} (1 - f_{\text{esc}}^{\text{ion}}) \dot{N}_{\text{ion}}. \quad (3)$$

Here, 0.68 represents the conversion probability for gas at  $10^4$  K, and  $f_{\text{esc}}^{\text{ion}}$  denotes the escape fraction of ionizing photons. In this work, we use the redshift-dependent galaxy escape fraction from Hayes et al. (2011), which is described by the relation:

$$f_{\text{esc}}^{\text{ion}} = 2.5 \times 10^{-3} \times (1+z)^{2.45}. \quad (4)$$

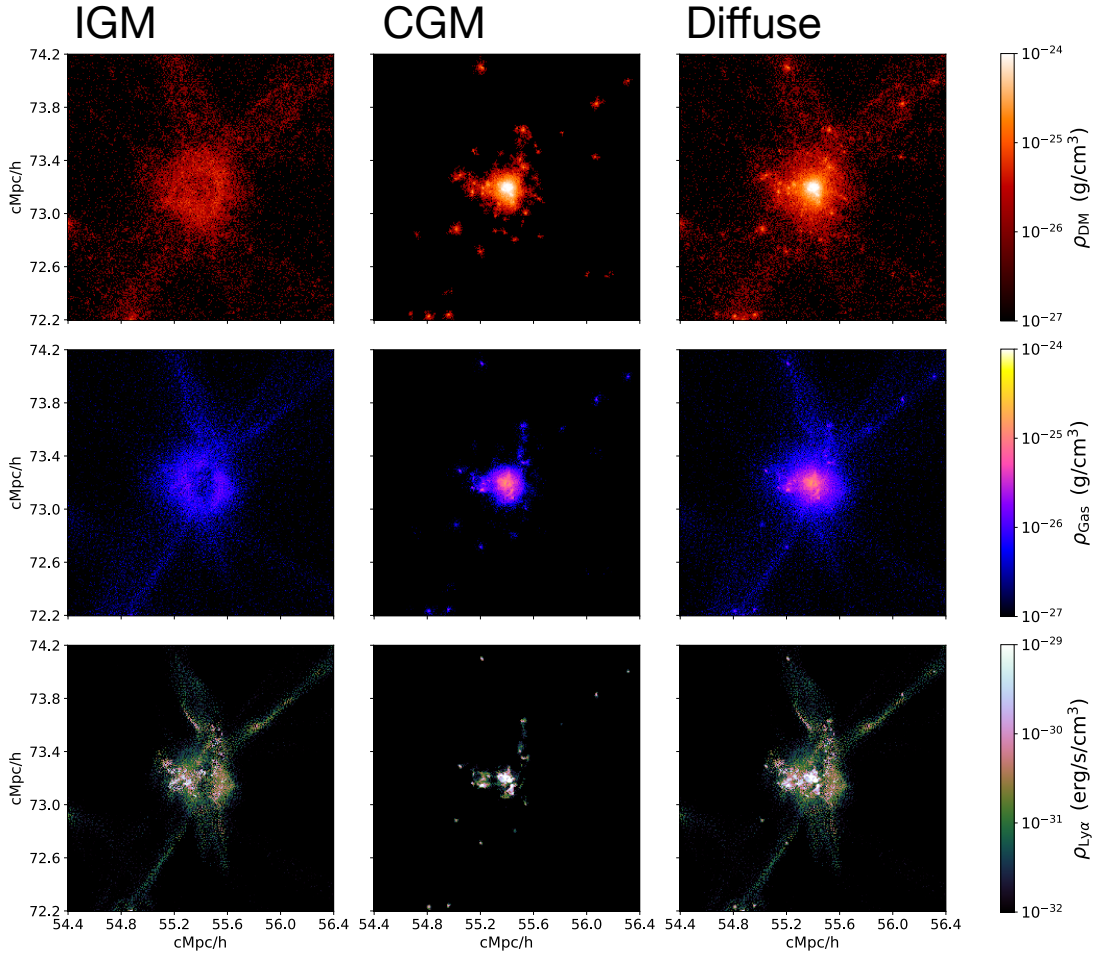


**Figure 2.** The top to bottom rows show the distribution of dark matter, gas, and Ly $\alpha$  emission within a  $1.44 \times 10^{12} M_{\odot}$  dark matter halo, centered in a cube box with a side length of 2 cMpc/h at  $z = 1$ . "IGM" column represents the region of IGM which connect halos throughout the universe, characterized by a lower average density than the CGM. "CGM" column represents the region of CGM, which closely surround galaxies and have stronger emission sources compared to the IGM. "Diffuse" column represents the region of diffuse gas which equals to "IGM" add "CGM" based on our definition.

The constant  $2.5 \times 10^{-3}$  was determined by constraining the galaxy escape fraction to be less than 30% at  $z = 6$ .  $\dot{N}_{ion}$  is the emission rate of ionizing photons from stars, which we calculate using the BPASS models (v2.2.1). These models provide a theoretical framework to interpret the integrated light from galaxies and stellar populations, with a particular focus on the effects of binary star systems (Eldridge et al. 2017). When calculating the Lyman-alpha emission from CGM and galaxy components, we multiply the emission by the galaxy escape fraction to account for the absorption effects in dense regions of the universe.

### 3. RESULTS

#### 3.1. Diffuse Gas Properties

We show the Ly $\alpha$  emission from diffuse gas based on TNG100-1 data in Figure 5. Recombination dominates the emission in low-density regions of  $n_{\text{H}} < 10^{-4} \text{ cm}^{-3}$ , while collisional excitation governs in relatively dense region of  $n_{\text{H}} > 10^{-4} \text{ cm}^{-3}$  at  $z = 1$  in both CGM and IGM components. The CGM component near the center of the halo has a higher density and dominates the Ly $\alpha$  emission of diffuse gas with  $n_{\text{H}} > 10^{-2.5}$ . In contrast, the IGM component, which is not associated with any halo structure, has a lower average density than the CGM. In regions where  $n_{\text{H}} < 10^{-3}$ , the IGM contributes more to the Ly $\alpha$  emission than the CGM.

Figure 6 illustrates the profiles of total Ly $\alpha$  luminosity from  $z = 5$  to  $z = 0$ . For any given  $z$ , the emission profile shows a sharp decrease at the tail of the lower density limit. At  $z > 3$ , Ly $\alpha$  luminosity mainly emits in gas of  $n > 10^{-6} \text{ cm}^{-3}$ . As  $z$  decreases, the

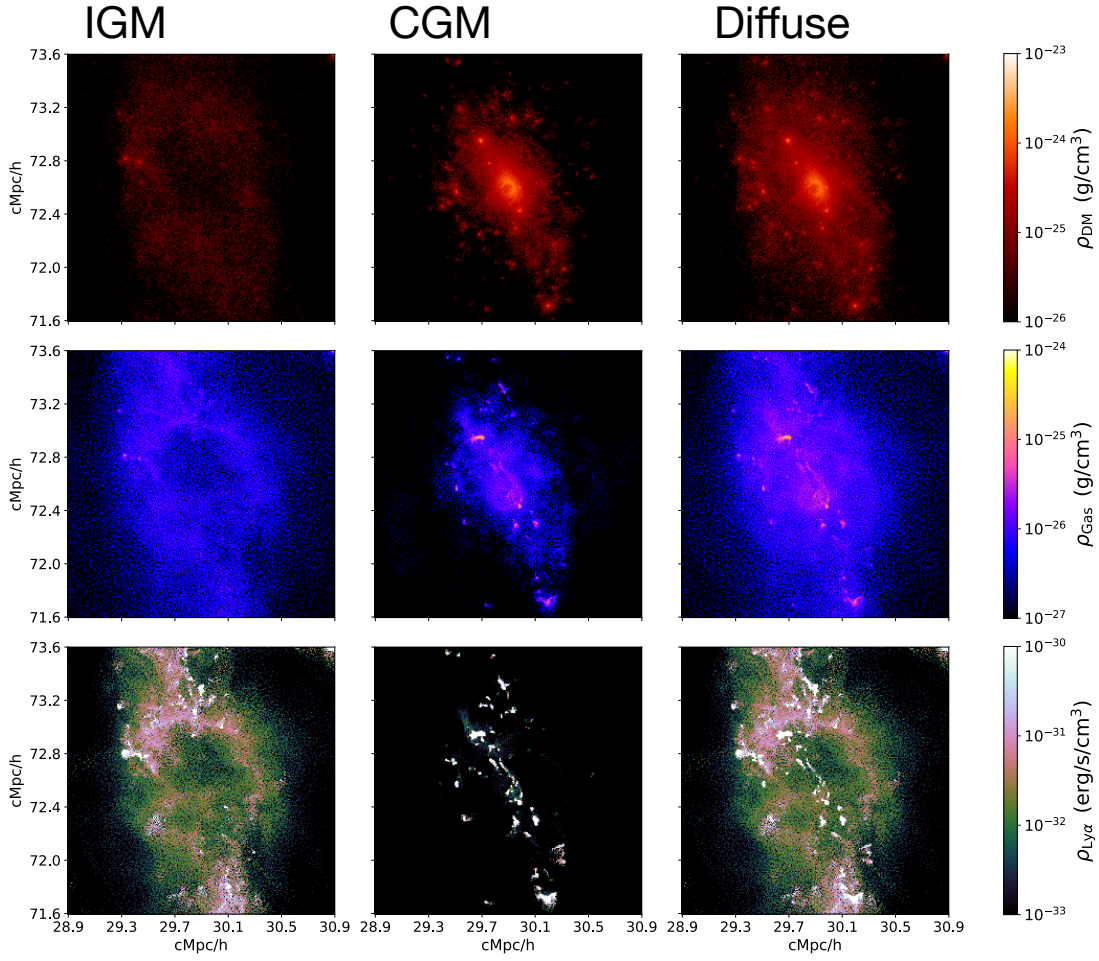


**Figure 3.** The top to bottom rows show the distribution of dark matter, gas, and  $\text{Ly}\alpha$  emission within a  $1.05 \times 10^{13} M_{\odot}$  dark matter halo, centered in a cube box with a side length of 2 cMpc/h at  $z = 1$ . "IGM" column represents the region of IGM which connect halos throughout the universe, characterized by a lower average density than the CGM. "CGM" column represents the region of CGM, which closely surround galaxies and have stronger emission sources compared to the IGM. "Diffuse" column represents the region of diffuse gas which equals to "IGM" add "CGM" based on our definition.

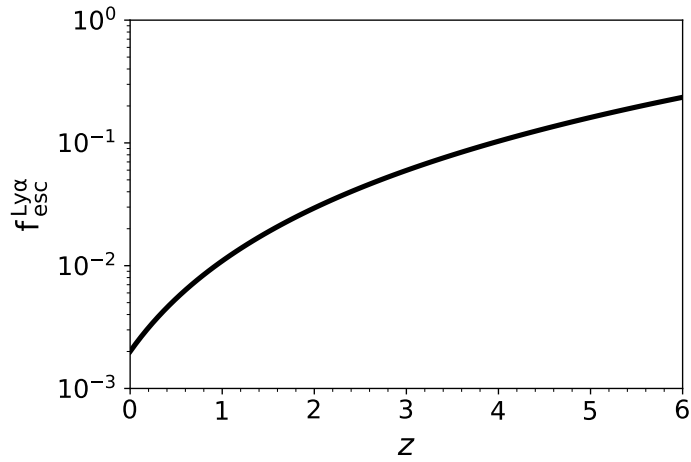


**Figure 4.** The redshift dependent galaxy escape fraction we used in calculating the  $\text{Ly}\alpha$  emission from galaxy and CGM components.

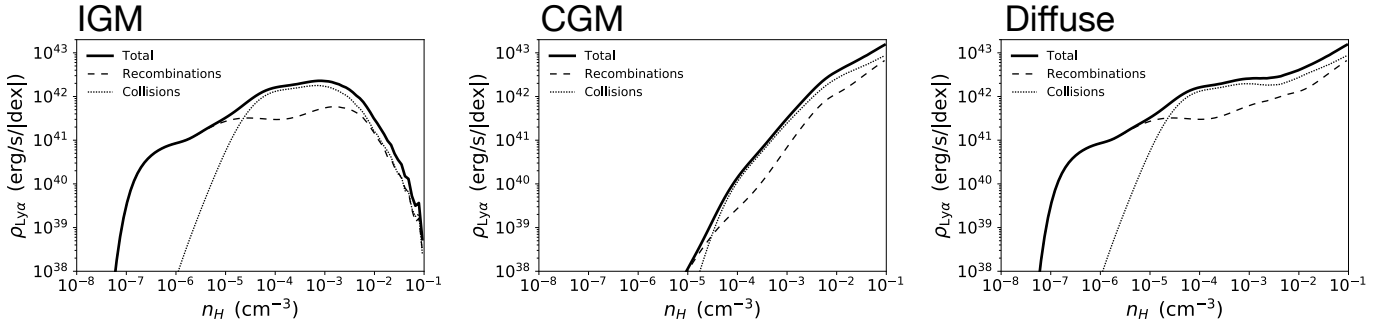


**Figure 5.** Ly $\alpha$  luminosity as a function of gas density ( $n$ ) at  $z = 1$  in diffuse gas. Collision emission mainly comes from  $n \approx 10^{-4.5} - 10^{-1} \text{ cm}^{-3}$ , while recombination emission from  $n_H \approx 10^{-7} - 10^{-4.5} \text{ cm}^{-3}$ .

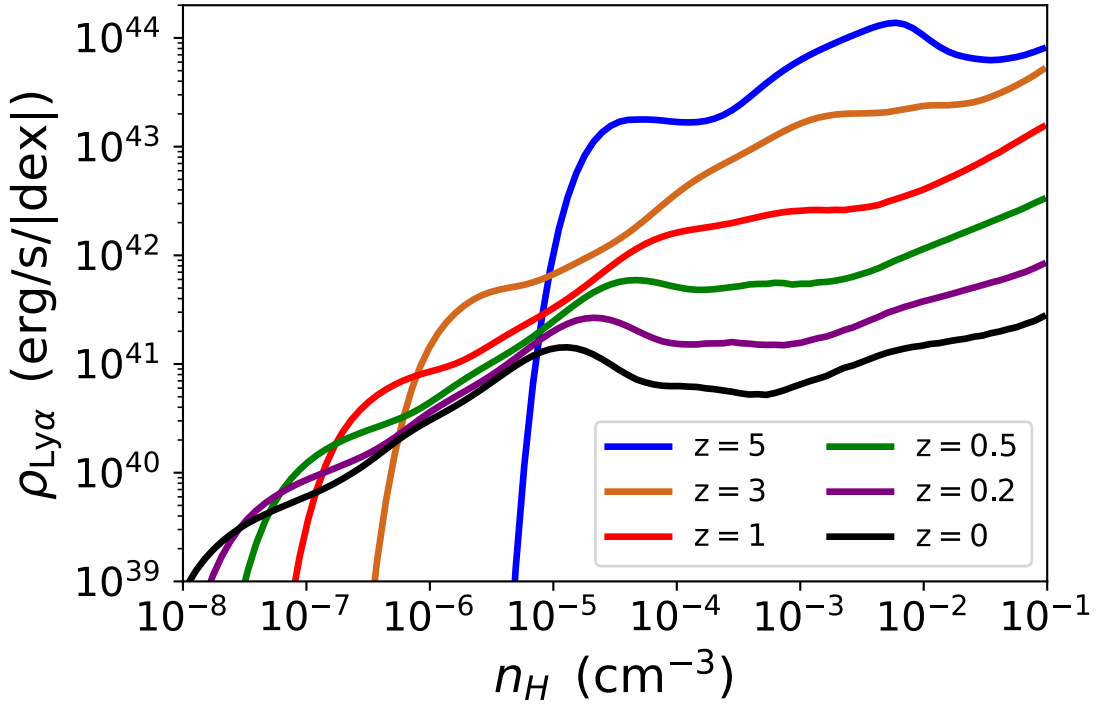


**Figure 6.** The evolution of Ly $\alpha$  luminosity function of diffuse gas from  $z = 6$  to  $z = 0$ .

emission rate becomes more even across gas of  $n_H = 10^{-7} - 10^{-2} \text{ cm}^{-3}$ . At  $z = 0$ , some of Ly $\alpha$  luminosity even comes from gas of  $n_H \leq 10^{-7} \text{ cm}^{-3}$

### 3.2. Gas Phase Diagrams

To better understand the Ly $\alpha$  emission from diffuse gas, we present the gas density-temperature-emission phase diagrams in Figure 7. In general, the Ly $\alpha$  emission mainly come from the gas of  $n_H \sim 10^{-8} - 10^{-1} \text{ cm}^{-3}$  and  $T \sim 10^2 - 10^8 \text{ K}$ . The diagram shifts toward lower gas density as  $z$  decreases. Especially, a tail in emission from recombination elongates to the gas of  $n_H < 10^{-5} \text{ cm}^{-3}$  and  $T < 10^4 \text{ K}$ .

### 3.3. Evolution of Ly $\alpha$ emissions across cosmic time

We define diffuse gas as comprising IGM and CGM components in Section 2.4. Figure 8 also delineates the Ly $\alpha$  luminosity density ( $\rho_{\text{Ly}\alpha}$ ) from IGMs, CGMs and galaxies. Tables 2 provides a breakdown of the  $\rho_{\text{Ly}\alpha}$  contributed from galaxies, CGM, and IGM, respectively. The diffuse  $\rho_{\text{Ly}\alpha}$  peaks at around  $z \sim 4$ . Compared to galaxies, the diffuse  $\rho_{\text{Ly}\alpha}$  at  $z \sim 1.5$  accounts for 11.2% of the total  $\rho_{\text{Ly}\alpha}$ , the highest contribution between  $z = 0$  and  $z = 6$ . At  $z = 0$ , the  $\rho_{\text{Ly}\alpha}$  is approximately 300 times weaker than at



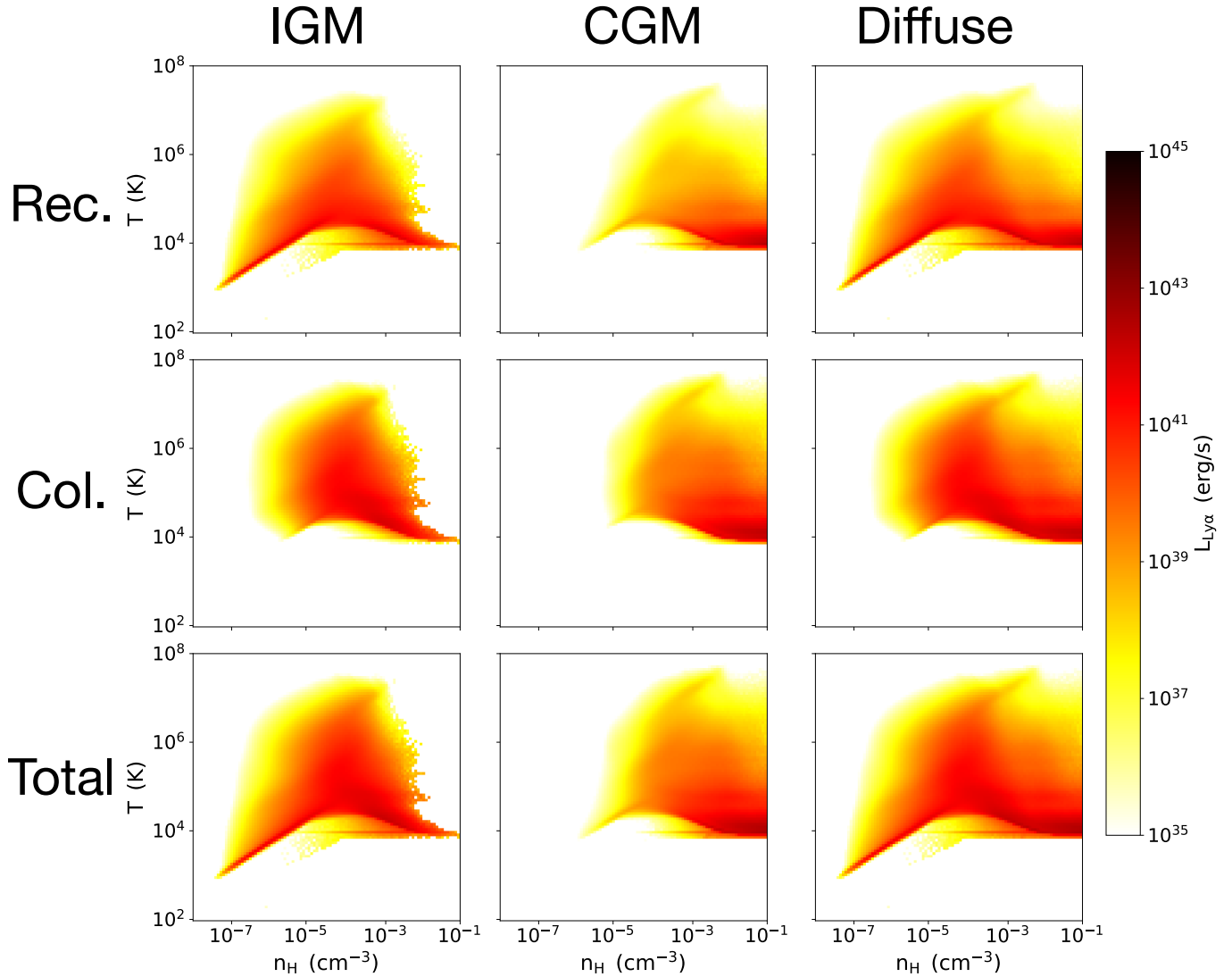


**Figure 7.** Density-temperature-emission diagram for diffuse gas at  $z = 0, 1, 3, 5$ . The region of strong  $\text{Ly}\alpha$  emission is located around  $T = 10^4$  and  $n_{\text{H}} = 10^{-6} - 10^{-2} \text{ cm}^{-3}$ . As the redshift decrease, the gas distribution shifts toward the left-bottom corner of diagram.

$z = 4$ . At  $z = 6$ , the  $\rho_{\text{Ly}\alpha}$  from the IGM component exceeds that of the CGM. However, at other redshifts, the contribution from the CGM component is 1.3 to 1.8 times larger than that of the IGM.

At  $z = 6$ , collisional excitation overwhelmingly dominates the  $\rho_{\text{Ly}\alpha}$ , surpassing the contribution from recombination by more than 100 times in the diffuse gas. However, by  $z = 5$ , the contribution from the recombination process becomes comparable to collisional excitation. For  $z = 0 - 5$ , the emission from collisional excitation is roughly 1.5 to 3 times stronger than that of recombination in the diffuse gas. For galaxy particles, the  $\text{Ly}\alpha$  emission primarily originates from the SFR and star components, contributing over 99% when  $z > 2$  and more than 95% at all redshifts. The contribution from collisional excitation and recombination processes in the galaxy region is negligible.

In Figure 9, we compare our results with observations and previous work. The TNG100-1 results indicate that  $\text{Ly}\alpha$  emission primarily originates from galaxies at any redshift. At  $z < 3$ , our  $\rho_{\text{Ly}\alpha}$  results are consistent with those of Wold et al. (2017). However, when compared with Chiang et al. (2019), which reports the total  $\rho_{\text{Ly}\alpha}$  at  $z = 0.3$  and  $z = 1$  using GALEX data through intensity mapping, our predictions are approximately 6 times smaller.

We estimate the observed upper limits of the IGM  $\rho_{\text{Ly}\alpha}$  by subtracting the integrated galaxy  $\rho_{\text{Ly}\alpha}$  from the total  $\rho_{\text{Ly}\alpha}$  values provided by Wold et al. (2017) and Chiang et al. (2019). Although the total  $\rho_{\text{Ly}\alpha}$  values fall within the range of predictions for integrated galaxy contributions, we can establish upper limits by subtracting the lower bounds of the integrated galaxy terms.

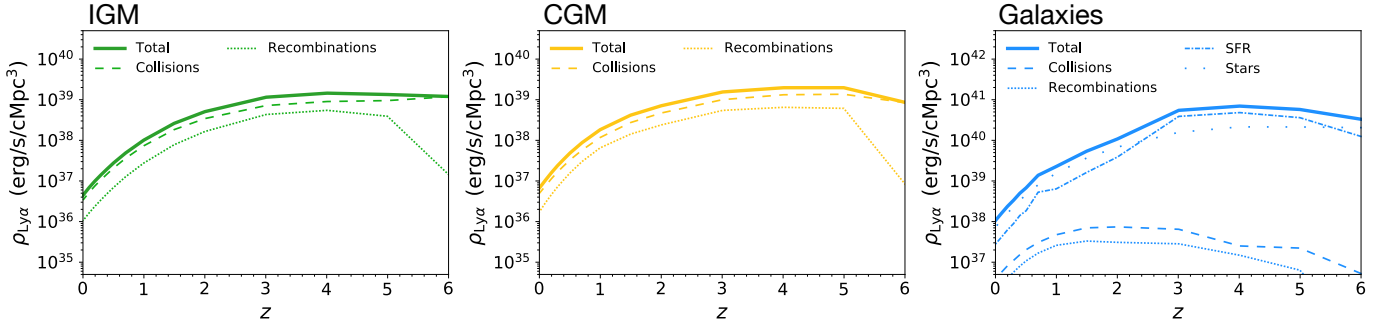


**Figure 8.** The panels left to right show the  $\text{Ly}\alpha$  emission contributed from collisional excitation and recombination process in IGM, CGM, and galaxies based on TNG100-1.

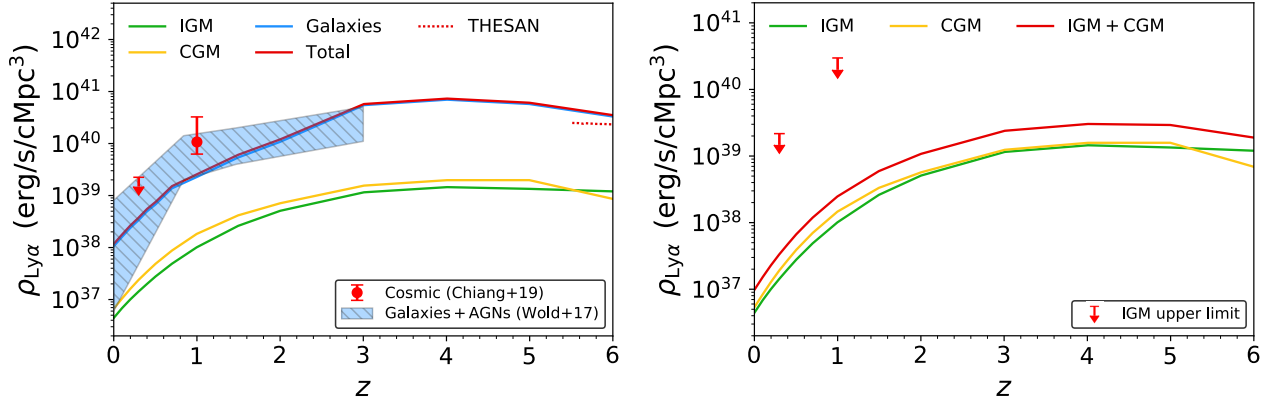


**Figure 9.** The evolution of comoving  $\rho_{\text{Ly}\alpha}$ .  $\rho_{\text{Ly}\alpha}$  increases with  $z$  and peaks around  $z \approx 4$ , then decrease with  $z$ . The left panel shows the  $\rho_{\text{Ly}\alpha}$  from the TNG100-1 and THESAN-1 data and compares it with recent observational results. Our predicted  $\rho_{\text{Ly}\alpha}$  is roughly 6 times weaker than the available observed  $\rho_{\text{Ly}\alpha}$ , containing  $\rho_{\text{Ly}\alpha}$  from galaxies, CGM, and diffuse gas. The right panel compares the  $\rho_{\text{Ly}\alpha}$  from IGM and CGM with the IGM upper limit based on Chiang et al. (2019); Wistok et al. (2021).

The right panel of Figure 9 displays these IGM upper limits and our diffuse  $\rho_{\text{Ly}\alpha}$  from TNG100-1. At  $z = 0.3$ , our diffuse  $\rho_{\text{Ly}\alpha}$  is 65 times smaller than the upper limit, and at  $z = 1$ , it is 120 times smaller than the upper limit.

Due to the challenges posed by observational limits and the low surface brightness of the diffuse  $\text{Ly}\alpha$  signal, direct detection proves to be challenging. However, our results suggest that  $\text{Ly}\alpha$  emission density would enhance as  $z$  increases. Thus, searching  $\text{Ly}\alpha$  emission from diffuse gas at  $z > 3$  may improve the probability of detection.

## 4. DISCUSSION

### 4.1. Comparison to previous theoretical studies

Investigating the physical properties of diffuse gas is crucial for unraveling the mysteries of the physical conditions within the IGM. Therefore, studying  $\text{Ly}\alpha$  emission from these diffuse gases holds significant value. Elias et al. (2020) explore the potential detectability of large-scale filaments. To isolate filament particles, they exclude any particles identified by FoF within a halo and then extract a  $5\text{cMpc}^2$  comoving region centered on the halo. When investigating the dependence of  $\text{Ly}\alpha$  emission on physical conditions at  $z = 3$ , they present temperature versus density phase-space diagrams. Compared with our results of phase diagrams, the morphology differs due to variations in data coverage. In their study, the selected particles represent the gas surrounding a halo, depicting the physical properties of a smaller cosmic volume. Instead, we consider the diffuse gas within the simulation box with  $100\text{cMpc}$  on a side, including IGM in the FoF groups. Thus, our phase diagrams can represent more general properties of diffuse gas. Their work also showed collisional excitation as the primary mechanism of diffuse  $\text{Ly}\alpha$  emission, which is consistent with our findings. Therefore, collisional excitation emerges as the key mechanism driving diffuse  $\text{Ly}\alpha$  emission in the high- $z$  universe.

Wistok et al. (2021) focused on studying  $\text{Ly}\alpha$  emission from IGM with galaxy clusters. Their analysis specifically considers gas well below the critical self-shielding density when calculating  $\text{Ly}\alpha$  emission due to collisional excitation. This critical

TNG100-1			
Redshift	Galaxies [erg/s/cMpc <sup>3</sup> ]	CGM [erg/s/cMpc <sup>3</sup> ]	IGM [erg/s/cMpc <sup>3</sup> ]
6	$2.68 \times 10^{40}$	$8.54 \times 10^{38}$	$1.20 \times 10^{39}$
5	$5.32 \times 10^{40}$	$1.98 \times 10^{39}$	$1.34 \times 10^{39}$
4	$6.69 \times 10^{40}$	$1.97 \times 10^{39}$	$1.45 \times 10^{39}$
3	$5.36 \times 10^{40}$	$1.55 \times 10^{39}$	$1.15 \times 10^{39}$
2	$1.06 \times 10^{40}$	$7.11 \times 10^{38}$	$5.09 \times 10^{38}$
1.5	$5.31 \times 10^{39}$	$4.16 \times 10^{38}$	$2.61 \times 10^{38}$
1	$2.25 \times 10^{39}$	$1.83 \times 10^{38}$	$1.01 \times 10^{38}$
0.7	$1.37 \times 10^{39}$	$8.75 \times 10^{37}$	$4.89 \times 10^{37}$
0.5	$6.74 \times 10^{38}$	$4.88 \times 10^{37}$	$2.78 \times 10^{37}$
0.4	$4.95 \times 10^{38}$	$3.42 \times 10^{37}$	$2.00 \times 10^{37}$
0.3	$3.35 \times 10^{38}$	$2.38 \times 10^{37}$	$1.42 \times 10^{37}$
0.2	$2.36 \times 10^{38}$	$1.60 \times 10^{37}$	$9.99 \times 10^{36}$
0.1	$1.60 \times 10^{38}$	$1.04 \times 10^{37}$	$6.83 \times 10^{36}$
0	$1.06 \times 10^{38}$	$6.70 \times 10^{36}$	$4.43 \times 10^{36}$

**Table 2.** The  $\text{Ly}\alpha$  luminosity density from Galaxies, CGM, and IGM based on TNG100-1. Depending on  $z$ , the  $\text{Ly}\alpha$  emission from galaxies is 2–150 stronger than that of diffuse gas.

self-shielding hydrogen number density is determined by setting  $T = 10^4$  K in Eq(13) as described by Rahmati et al. (2013). Essentially, this critical self-shielding density acts as a threshold, similar to imposing a predefined number overdensity cut. By applying this overdensity cut, the contribution from collisional excitation is reduced because the high-dense region, largely contributing to emission from collision excitation, has been removed. Their results exhibit distinct redshift evolutions of the comoving  $\text{Ly}\alpha$  luminosity density compared to our findings, particularly concerning collisional excitation. This discrepancy implies the importance of considering "different density regimes and selection criteria" when evaluating the  $\text{Ly}\alpha$  emission properties of the IGM. The results are sensitive to the methods used for identifying IGM gas.

#### 4.2. Outlook for future $\text{Ly}\alpha$ surveys

Recent surveys using integral field unit (IFU) spectrographs on 8–10m class ground-based telescopes, such as MUSE, KCWI, and HETDEX (Bacon et al. 2010; Chen et al. 2021; Davis et al. 2023), have made it possible to study individual, faint  $\text{Ly}\alpha$  halos. The detection of filamentary  $\text{Ly}\alpha$  emission around galaxies reveals the diffuse gas believed to fuel galaxy growth (Umehata et al. 2019b; Martin et al. 2019).  $\text{Ly}\alpha$  emission serves as a powerful cosmological tool, helping to uncover the mysteries of the early universe.

Upcoming 30m class telescopes will further enhance the detection of  $\text{Ly}\alpha$  filaments (Byrohl & Nelson 2023), providing deeper insight into the large-scale structure of the universe and the distribution of the cosmic web. The next-generation MUSE-like observatory, the European Extremely Large Telescope (E-ELT), with its long exposure capabilities, will allow for more detailed analyses (Witstok et al. 2021). Similarly, other 30m class telescopes like the Thirty Meter Telescope (TMT) and the Giant Magellan Telescope (GMT) will enable the statistical detection of faint  $\text{Ly}\alpha$  emission from galaxies at  $z \sim 10$  (Yajima et al. 2018). These surveys will offer valuable insights into the processes governing cosmic reionization, star formation rates, and galactic feedback mechanisms.

## 5. CONCLUSION

We present a systematic study of  $\text{Ly}\alpha$  emission from cosmic diffuse gas, including CGM and IGM, based on the IllustrisTNG project. We begin by identifying diffuse gas within cosmological simulation models by utilizing the FoF and Subfind algorithms. Then, we calculate their  $\text{Ly}\alpha$  luminosity by considering the collisional excitation and recombination processes of hydrogen based on the local gas properties. Our results show that collisional excitation predominantly governs the overall  $\text{Ly}\alpha$  luminosity, exhibiting robust emission capabilities in regions of gas of  $n_{\text{H}} \sim 10^{-5} - 10^{-2} \text{cm}^{-3}$  and  $T \sim 10^4 - 10^6$  K. Besides, the recombination process, occurring in more dilute gas of  $n_{\text{H}} \sim 10^{-5} - 10^{-8} \text{cm}^{-3}$  and  $T \sim 10^4$  K, yields a weaker  $\text{Ly}\alpha$  emission. Furthermore, the redshift evolution of comoving  $\text{Ly}\alpha$  luminosity suggests that the contribution from the CGM

components is 1.3 to 1.8 times larger than that of the IGM. Based on the intensity mapping results as shown in the right panel of Figure 9, our predicted Ly $\alpha$  emission from diffuse gas agrees with the observed cosmic Ly $\alpha$  emission at  $z = 0.3$ , and  $z = 1$ . However, our results suggest that Ly $\alpha$  emission density increases toward higher  $z$ . Thus, future observatories may hold a great promise to detect Ly $\alpha$  emission from diffuse gas at  $z = 3 - 5$ .

This research is supported by the National Science and Technology Council, Taiwan, under grant No. MOST 110-2112-M-001-068-MY3, NSTC 113-2112-M-001-028-, and the Academia Sinica, Taiwan, under a career development award under grant No. AS-CDA-111-M04. This research was supported in part by grant NSF PHY-2309135 to the Kavli Institute for Theoretical Physics (KITP) and grant NSF PHY-2210452 to the Aspen Center for Physics. Our computing resources were supported by the National Energy Research Scientific Computing Center (NERSC), a U.S. Department of Energy Office of Science User Facility operated under Contract No. DE-AC02-05CH11231 and the TIARA Cluster at the Academia Sinica Institute of Astronomy and Astrophysics (ASIAA).

## REFERENCES

- Angulo, R. E., & Hahn, O. 2022, *Living Reviews in Computational Astrophysics*, 8, 1
- Bacon, R., Accardo, M., Adjali, L., et al. 2010, in *Ground-based and Airborne Instrumentation for Astronomy III*, Vol. 7735, SPIE, 131
- Bacon, R., Mary, D., Garel, T., et al. 2021, *A&A*, 647, A107
- Bagla, J. S. 2002, *Journal of Astrophysics and Astronomy*, 23, 185
- Behrens, C., Byrohl, C., Saito, S., & Niemeyer, J. C. 2018, *A&A*, 614, A31
- Bode, P., & Ostriker, J. P. 2003, *ApJS*, 145, 1
- Böhringer, H., & Werner, N. 2010, *A&A Rv*, 18, 127
- Bond, J. R., Kofman, L., & Pogosyan, D. 1996, *Nature*, 380, 603
- Byrohl, C., & Nelson, D. 2023, *MNRAS*, 523, 5248
- Byrohl, C., Nelson, D., Behrens, C., et al. 2021, *MNRAS*, 506, 5129
- Cantalupo, S., Porciani, C., & Lilly, S. J. 2008, *ApJ*, 672, 48
- Cantalupo, S., Porciani, C., Lilly, S. J., & Miniati, F. 2005, *ApJ*, 628, 61
- Chabrier, G. 2003, *PASP*, 115, 763
- Charlot, S., & Fall, S. M. 1993, *ApJ*, 415, 580
- Chen, Y., Steidel, C. C., Erb, D. K., et al. 2021, *MNRAS*, 508, 19
- Chiang, Y.-K., Ménard, B., & Schiminovich, D. 2019, *ApJ*, 877, 150
- Crain, R. A., Theuns, T., Dalla Vecchia, C., et al. 2009, *MNRAS*, 399, 1773
- Davis, D., Gebhardt, K., Cooper, E. M., et al. 2023, *ApJ*, 954, 209
- Dubois, Y., Pichon, C., Welker, C., et al. 2014, *MNRAS*, 444, 1453
- Eldridge, J. J., Stanway, E. R., Xiao, L., et al. 2017, *PASA*, 34, e058
- Elias, L. M., Genel, S., Sternberg, A., et al. 2020, *MNRAS*, 494, 5439
- Gallego, S. G., Cantalupo, S., Lilly, S., et al. 2018, *MNRAS*, 475, 3854
- Garaldi, E., Kannan, R., Smith, A., et al. 2022, *MNRAS*, 512, 4909
- Gronke, M., & Bird, S. 2017, *ApJ*, 835, 207
- Gunn, J. E., & Gott, J. Richard, I. 1972, *ApJ*, 176, 1
- Hasan, F., Burchett, J. N., Abeyta, A., et al. 2023, *ApJ*, 950, 114
- Hayes, M., Schaerer, D., Östlin, G., et al. 2011, *ApJ*, 730, 8
- Hill, G. J., Gebhardt, K., Komatsu, E., et al. 2008, in *Astronomical Society of the Pacific Conference Series*, Vol. 399, *Panoramic Views of Galaxy Formation and Evolution*, ed. T. Kodama, T. Yamada, & K. Aoki, 115
- Hogan, C. J., & Weymann, R. J. 1987, *MNRAS*, 225, 1P
- Hu, E. M., Songaila, A., Cowie, L. L., & Stockton, A. 1991, *ApJ*, 368, 28
- Kannan, R., Garaldi, E., Smith, A., et al. 2022, *MNRAS*, 511, 4005
- Kraljic, K., Arnouts, S., Pichon, C., et al. 2018, *MNRAS*, 474, 547
- Lee, M. M., Schimek, A., Cicone, C., et al. 2024, *arXiv e-prints*, arXiv:2403.00924
- Mantz, A. B., Allen, S. W., Morris, R. G., et al. 2017, *MNRAS*, 472, 2877
- Marinacci, F., Vogelsberger, M., Pakmor, R., et al. 2018, *MNRAS*, 480, 5113
- Martin, D. C., Chang, D., Matuszewski, M., et al. 2014, *ApJ*, 786, 107
- Martin, D. C., Darvish, B., Lin, Z., et al. 2023, *Nature Astronomy*, 7, 1390
- Martin, D. C., O’Sullivan, D., Matuszewski, M., et al. 2019, *Nature Astronomy*, 3, 822
- McCarthy, I. G., Schaye, J., Bird, S., & Le Brun, A. M. C. 2017, *MNRAS*, 465, 2936
- McQuinn, M. 2016, *ARA&A*, 54, 313
- Naiman, J. P., Pillepich, A., Springel, V., et al. 2018, *MNRAS*, 477, 1206
- Nelson, D., Pillepich, A., Springel, V., et al. 2018, *MNRAS*, 475, 624
- . 2019a, *MNRAS*, 490, 3234
- Nelson, D., Springel, V., Pillepich, A., et al. 2019b, *Computational Astrophysics and Cosmology*, 6, 2
- Ouchi, M. 2019, *Saas-Fee Advanced Course*, 46, 189

- Pakmor, R., Bauer, A., & Springel, V. 2011, *MNRAS*, 418, 1392
- Pakmor, R., & Springel, V. 2013, *MNRAS*, 432, 176
- Pakmor, R., van de Voort, F., Bieri, R., et al. 2020, *MNRAS*, 498, 3125
- Peebles, P. J. E. 1980, The large-scale structure of the universe
- Peebles, M., Behroozi, P., Bordoloi, R., et al. 2019, *BAAS*, 51, 368
- Pillepich, A., Nelson, D., Hernquist, L., et al. 2018a, *MNRAS*, 475, 648
- Pillepich, A., Springel, V., Nelson, D., et al. 2018b, *MNRAS*, 473, 4077
- Pillepich, A., Nelson, D., Springel, V., et al. 2019, *MNRAS*, 490, 3196
- Planck Collaboration, Ade, P. A. R., Aghanim, N., et al. 2016, *A&A*, 594, A13
- Rahmati, A., Pawlik, A. H., Raičević, M., & Schaye, J. 2013, *MNRAS*, 430, 2427
- Renard, P., Spinoso, D., Sun, Z., et al. 2024, *arXiv e-prints*, arXiv:2406.18775
- Roche, N., Humphrey, A., & Binette, L. 2014, *MNRAS*, 443, 3795
- Rosdahl, J., & Blaizot, J. 2012, *MNRAS*, 423, 344
- Sarazin, C. L. 1986, *Reviews of Modern Physics*, 58, 1
- Scholz, T. T., & Walters, H. R. J. 1991, *ApJ*, 380, 302
- Smith, A., Kannan, R., Garaldi, E., et al. 2022, *Monthly Notices of the Royal Astronomical Society*, 512, 3243
- Smith, A., Ma, X., Bromm, V., et al. 2019, *MNRAS*, 484, 39
- Smith, B., Sigurdsson, S., & Abel, T. 2008, *MNRAS*, 385, 1443
- Springel, V. 2010, *MNRAS*, 401, 791
- Springel, V., & Hernquist, L. 2003, *MNRAS*, 339, 289
- Springel, V., White, S. D. M., Tormen, G., & Kauffmann, G. 2001, *MNRAS*, 328, 726
- Springel, V., White, S. D. M., Jenkins, A., et al. 2005, *Nature*, 435, 629
- Springel, V., Pakmor, R., Pillepich, A., et al. 2018, *MNRAS*, 475, 676
- Steidel, C. C., Giavalisco, M., Pettini, M., Dickinson, M., & Adelberger, K. L. 1996, *ApJL*, 462, L17
- Tapken, C., Appenzeller, I., Noll, S., et al. 2007, *A&A*, 467, 63
- Torrey, P., Vogelsberger, M., Genel, S., et al. 2014, *MNRAS*, 438, 1985
- Tozzi, P., & Norman, C. 2001, *ApJ*, 546, 63
- Tumlinson, J., Peebles, M. S., & Werk, J. K. 2017, *ARA&A*, 55, 389
- Umehata, H., Fumagalli, M., Smail, I., et al. 2019a, *Science*, 366, 97
- . 2019b, *Science*, 366, 97
- Vogelsberger, M., Genel, S., Sijacki, D., et al. 2013, *MNRAS*, 436, 3031
- Vogelsberger, M., Marinacci, F., Torrey, P., & Puchwein, E. 2020, *Nature Reviews Physics*, 2, 42
- Wang, L., Dutton, A. A., Stinson, G. S., et al. 2015, *MNRAS*, 454, 83
- Weinberger, R., Springel, V., Hernquist, L., et al. 2017, *MNRAS*, 465, 3291
- Wiersma, R. P. C., Schaye, J., & Smith, B. D. 2009, *MNRAS*, 393, 99
- Witstok, J., Puchwein, E., Kulkarni, G., Smit, R., & Haehnelt, M. G. 2021, *A&A*, 650, A98
- Wold, I. G. B., Finkelstein, S. L., Barger, A. J., Cowie, L. L., & Rosenwasser, B. 2017, *ApJ*, 848, 108
- Xu, G. 1995, *ApJS*, 98, 355
- Yajima, H., Sugimura, K., & Hasegawa, K. 2018, *MNRAS*, 477, 5406
- Yuan, F., & Narayan, R. 2014, *ARA&A*, 52, 529